

Characterization of Microstructure and Texture in Grain-Oriented High Silicon Steel by Strip Casting

Xiang Lu¹ · Yun-Bo Xu¹ · Feng Fang¹ · Yuan-Xiang Zhang¹ · Yang Wang¹ · Hai-Tao Jiao¹ · R. D. K. Misra² · Guang-Ming Cao¹ · Cheng-Gang Li¹ · Guo-Dong Wang¹

Received: 2 July 2015 / Revised: 26 October 2015 / Published online: 17 November 2015
© The Chinese Society for Metals and Springer-Verlag Berlin Heidelberg 2015

Abstract Grain-oriented 4.5 wt% Si and 6.5 wt% Si steels were produced by strip casting, warm rolling, cold rolling, primary annealing, and secondary annealing. Goss grains were sufficiently developed and covered the entire surface of the secondary recrystallized sheets. The microstructure and texture was characterized by OM, EBSD, TEM, and XRD. It was observed that after rolling at 700 °C, the 6.5 wt% Si steel exhibited a considerable degree of shear bands, whereas the 4.5 wt% Si steel indicated their rare presence. After primary annealing, completely equiaxed grains showing strong γ -fiber texture were presented in both alloys. By comparison, the 6.5 wt% Si steel showed smaller grain size and few favorable Goss grains. Additionally, a higher density of fine precipitates were exhibited in the 6.5 wt% Si steel, leading to a ~ 30 -s delay in primary recrystallization. During secondary annealing, abnormal grain growth of the 6.5 wt% Si steel occurred at higher temperature compared to the 4.5 wt% Si steel, and the final grain size of the 6.5 wt% Si steel was greater. The magnetic induction B_8 of the 4.5 wt% Si and the 6.5 wt% Si steels was 1.75 and 1.76 T, respectively, and the high-frequency core losses were significantly improved in comparison with the non-oriented high silicon steel.

KEY WORDS: Strip casting; Grain-oriented high silicon steel; Microstructure; Texture

1 Introduction

Grain-oriented silicon steel is regarded as an excellent core material for transformers and other electrical devices because of perfect magnetic properties and low cost [1, 2]. The silicon content of commercial grain-oriented silicon steel is restricted to <3.5 wt% in order to ensure the ductility [3, 4]. In general, superior magnetic properties are

obtained at higher silicon content (4.0 wt%–6.5 wt%), especially at ~ 6.5 wt%, a content that exhibits low core losses and near-zero magnetostriction [5, 6]. However, additional silicon content significantly decreases the workability of the alloy, limiting the application of such grain-oriented high silicon steel. To overcome the poor workability, several methods have been proposed. Arai et al. [7] reported that the grain-oriented Fe-4.5 wt% Si steel can be made by rapid quenching method followed by a cold rolling and annealing. This method consumed excessive energy as 200 cold rolling passes were needed. Honma and coworker [5, 8, 9] proposed an approach to fabricate ultrahigh silicon steel (4.5 wt%–7.1 wt% Si) by conventional rolling way. But the rolling strategy was complicated, and a nitriding treatment was necessary. In addition, several researchers [10–14] fabricated the grain-oriented high silicon steel by siliconizing and long-term diffusion treatment initial from conventional low-silicon steel, termed as chemical vapor deposition (CVD) method.

Available online at <http://link.springer.com/journal/40195>.

✉ Xiang Lu
lx_neu@126.com

¹ State Key Laboratory of Rolling and Automation, Northeastern University, Shenyang 110819, China

² Laboratory for Excellence in Advanced Steel Research, Department of Metallurgical, Materials and Biomedical Engineering, University of Texas at El Paso, El Paso, TX 79912, USA

Table 1 Chemical composition of the silicon steels

Steel	Si	C	Mn	S	Al	N	Nb	Fe
4.5Si	4.48	<0.003	0.225	0.021	0.011	0.007	0.031	Bal.
6.5Si	6.45	<0.003	0.250	0.020	0.012	0.010	0.041	Bal.

All the methods mentioned above involve complicated procedure; thus, simplified process is required.

Strip casting is a method that produces steel strip of 2–4 mm thickness from the liquid metal, which eliminates the slab casting and hot rolling process. It has the advantages of processing the grain-oriented high silicon steel due

to the reduced thickness and homogeneous initial microstructure as a result of rapid cooling rate. So far, few research work have been carried out on strip casting high silicon steel, and the limited published papers mainly deal with the as-cast strip and non-oriented silicon steel. Park *et al.* [15–17] reported the initial microstructure and texture of the Fe-4.3 wt% Si and the Fe-4.5 wt% Si steels by strip casting for the first time, and pointed out that the microstructure and texture of as-cast strip was related to superheating. Liu *et al.* [18] reported that hot rolling introduced prior to the warm rolling decreased the detrimental recrystallized γ -fiber texture in the non-oriented Fe-

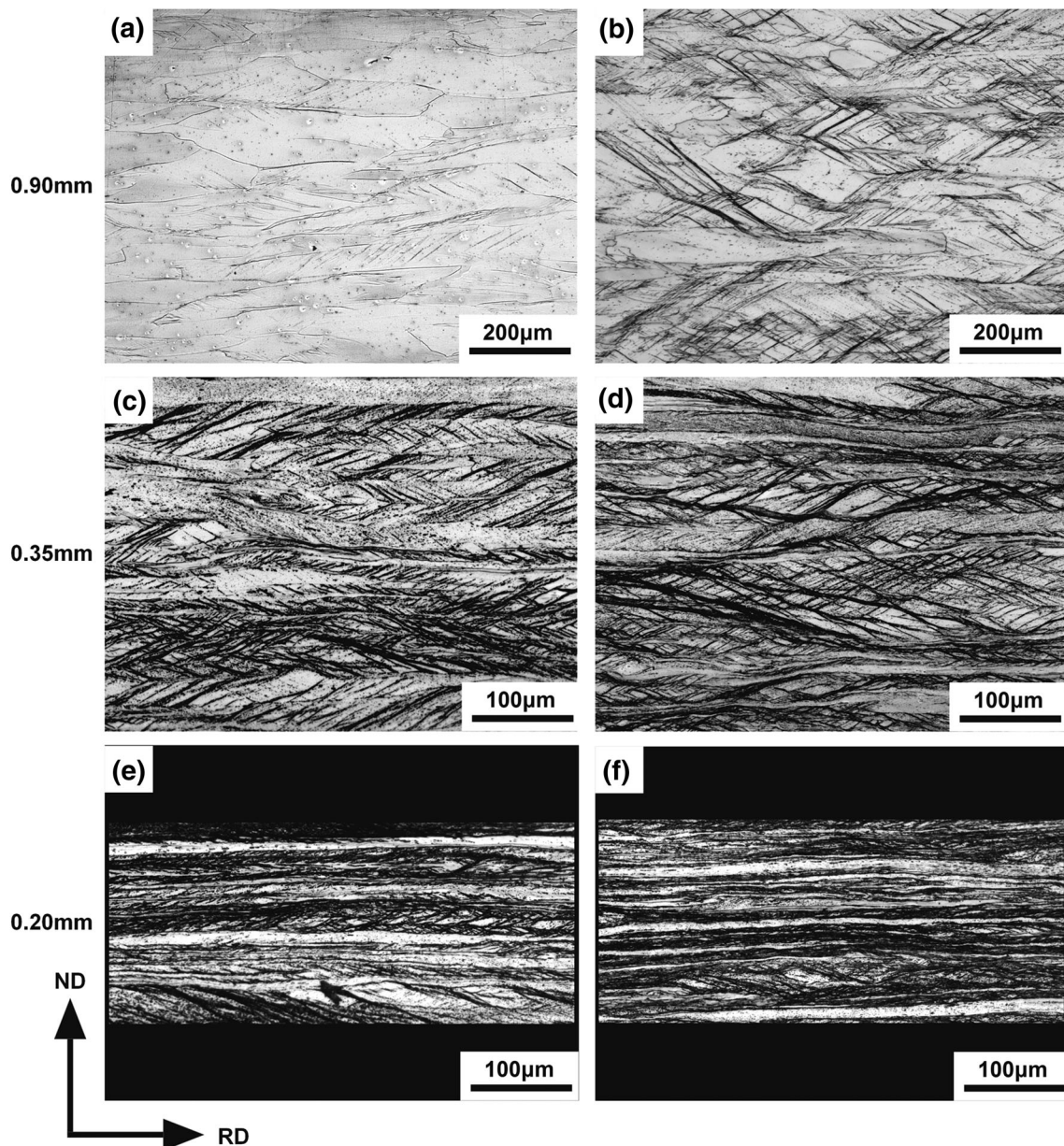


Fig. 1 As-rolled microstructures of the 4.5Si steel **a, c, e** and the 6.5Si steel **b, d, f**

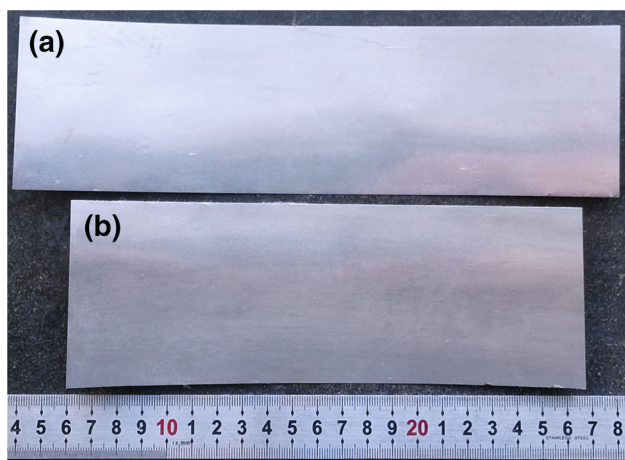


Fig. 2 Final cold-rolled sheets of the 4.5Si **a** and the 6.5Si **b** steels

6.2 wt% Si steel by strip casting. Li *et al.* [19] fabricated the non-oriented Fe-6.5 wt% Si steel characterized by strong favorable λ -fiber texture after annealing by strip casting, and proposed that dominant λ -fiber texture in the as-cast strip would give rise to λ -fiber texture in the final sheet. The microstructure and texture of the grain-oriented high silicon steel is different and has not been reported. Also, no attention is given to secondary recrystallization process, and the secondary recrystallization behavior of the grain-oriented high silicon steel continues to be unclear.

In the present study, the grain-oriented 4.5 wt% Si steel and the grain-oriented 6.5 wt% Si steel were prepared by strip casting, warm rolling, cold rolling, primary annealing, and secondary annealing. The microstructure, texture, and precipitates produced during deformation and recrystallization were characterized.

2 Experiment Procedure

Two strips of 110 mm width and 2.3 mm thickness containing ~ 4.5 wt% Si (denoted by 4.5Si) and ~ 6.5 wt% Si (denoted by 6.5Si) were produced by a twin-roll strip caster, as described earlier [20, 21]. The chemical

composition is presented in Table 1. The as-cast strips were annealed at 1050 °C for 5 min and warm-rolled to 0.90 mm at 700 °C, then warm-rolled to 0.35 mm at 400 °C, and finally, cold-rolled to 0.20 mm. Primary annealing was performed at 850 °C for 5 min in dry 100% N₂ atmosphere. Some partial tests for recrystallization were carried out at 850 °C to determine the primary recrystallization rate. The secondary annealing was carried out from 830 to 1200 °C at a heating rate of 15 °C/h in 25% H₂ + 75% N₂ atmosphere, and maintained for 20 h under 100% H₂ for purification. During secondary annealing, the specimens were extracted at different temperatures at the intervals of 20 °C from 900 to 1200 °C to determine the onset of secondary recrystallization temperature.

The microstructure of the specimens was observed by optical microscopy (OM) after etching with 5 g CuSO₄ + 40 mL HCl + 80 mL H₂O. The textures of the as-rolled sheet and primary annealed sheet were examined by Bruker D8 X-ray diffractometer. The orientation distribution functions (ODFs) were calculated from the {110}, {200}, and {211} incomplete pole figures obtained from XRD data. The microhardness of the partial recrystallized specimens was measured using Future-Tech machine at a 4.9-N load and 10-s dwell time. The second-phase particles in the primary annealed sheet were observed and identified by Tecnai G2 TEM. The grain orientation of the primary and secondary annealed sheets was examined by OIM 4000 EBSD system available with FEI Quanta 600 SEM, and the secondary recrystallized textures were calculated based on the results of six specimens. The magnetic induction at 800 A/m (B_8), and core losses at 1.0 T by 400 Hz ($P_{10/400}$) and 1000 Hz ($P_{10/1k}$) of the specimens (100 mm in rolling direction and 30 mm in transverse direction) were measured using single sheet tester.

3 Results and Discussion

3.1 Rolling

By adopting a relatively low melt superheating in the present work [22], two starting materials, namely the 4.5Si

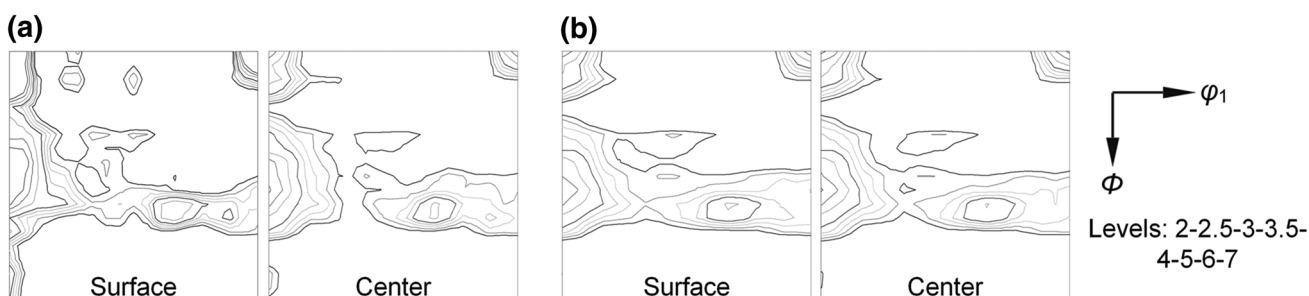


Fig. 3 Textures of the 4.5Si **a** and the 6.5Si **b** steels after final cold rolling

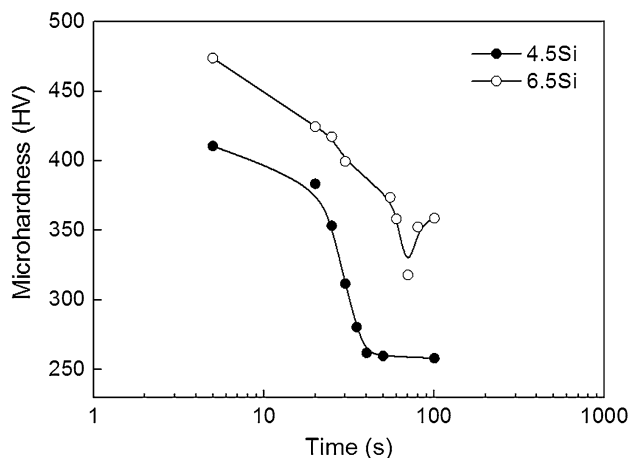


Fig. 4 Microhardness evolution for the 4.5Si and the 6.5Si steels during primary annealing

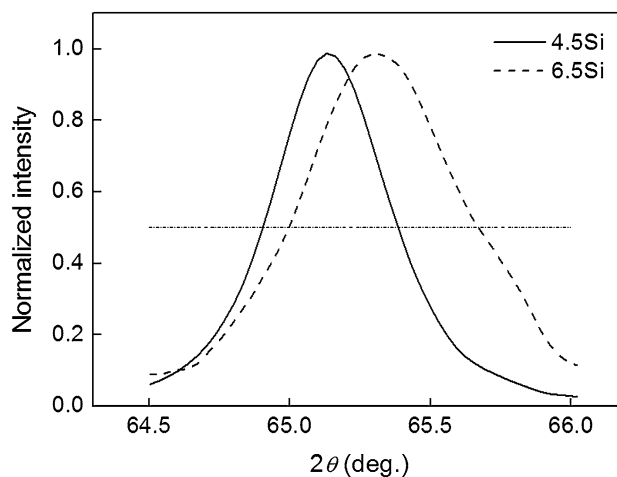


Fig. 6 {200} XRD peak profiles for the 4.5Si and the 6.5Si cold-rolled sheets

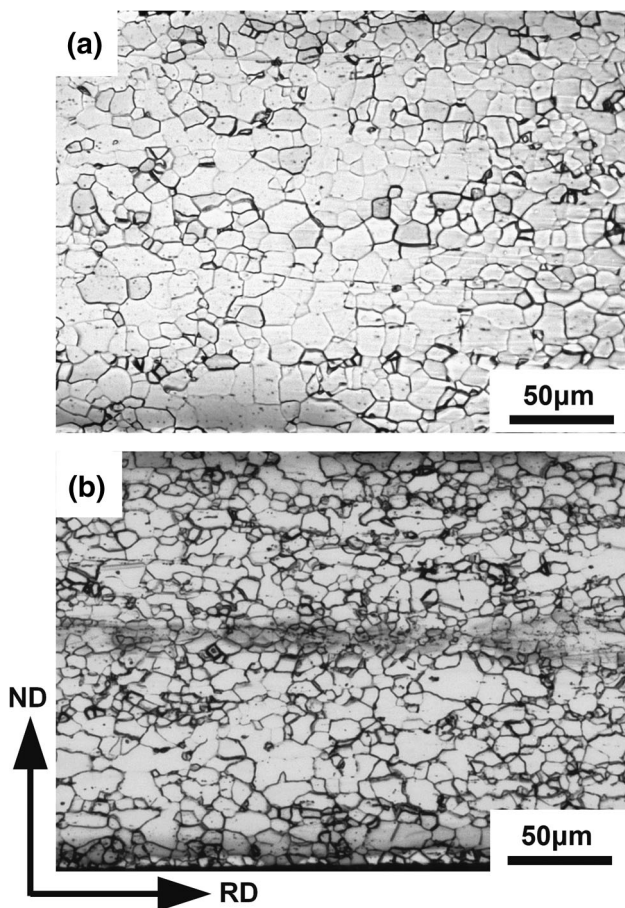


Fig. 5 Microstructures of the 4.5Si **a** and the 6.5Si **b** primary annealed sheets

and the 6.5Si as-cast strips, were characterized by equiaxed grain structure and random texture. The average sizes were ~ 190 and ~ 150 μm , respectively. After warm rolling at 700 $^{\circ}\text{C}$, both silicon sheets exhibited elongated grains

together with shear bands (Fig. 1a, b). Compared with the 4.5Si sheet, the 6.5Si sheet indicated a considerable amount of shear bands, which was attributed to the ordering phenomenon. According to the phase diagram [23], the 6.5Si steel has B2 ordered structure at 700 $^{\circ}\text{C}$. Thus, the perfect dislocation a $\langle 111 \rangle$ in the 6.5Si steel tends to resolve into two partial dislocations of $a/2\langle 111 \rangle$ bounded with anti-phase boundary (APB) [24]. These partial dislocations have poor mobility to cross-slip or climb, leading to strong work hardening effect and destabilizes deformation while shear-band formation is promoted [25] (Fig. 1b). In contrast, the 4.5Si steel is deformed in the disordered state that the perfect dislocations with good mobility are presented. Therefore, relatively stable deformation is obtained such that shear bands are rare (Fig. 1a). A similar result was obtained in Ni_3Fe alloy after rolling in both ordered and disordered states [26]. Subsequently, when were rolled to 0.35 mm, both the 4.5Si and the 6.5Si steels were characterized by elongated grains accompanied by massive shear bands, as shown in Fig. 1c, d. No obvious differences were observed in terms of optical microstructure. After final cold rolling to 0.2 mm, both the 4.5Si and the 6.5Si sheets exhibited pancake-shaped grains with boundary parallel to the rolling direction. By comparison, the 6.5Si steel had a narrow grain structure, as shown in Fig. 1e, f.

When the 6.5Si alloy was deformed, its order was destroyed because of the formation of new APB tracks behind imperfect gliding super dislocations [27], referred as strain-induced disordering. This means that more severe plastic deformation occurs in the 6.5Si steel. In the present work, 3-stage rolling strategy was adopted to progressively destroy the order, making cold rolling to 0.2 mm possible. Figure 2 shows the final cold-rolled sheets of the 4.5Si (a) and the 6.5Si (b) steels. No pronounced cracks were seen, indicating excellent ductility of 0.35 -mm warm-

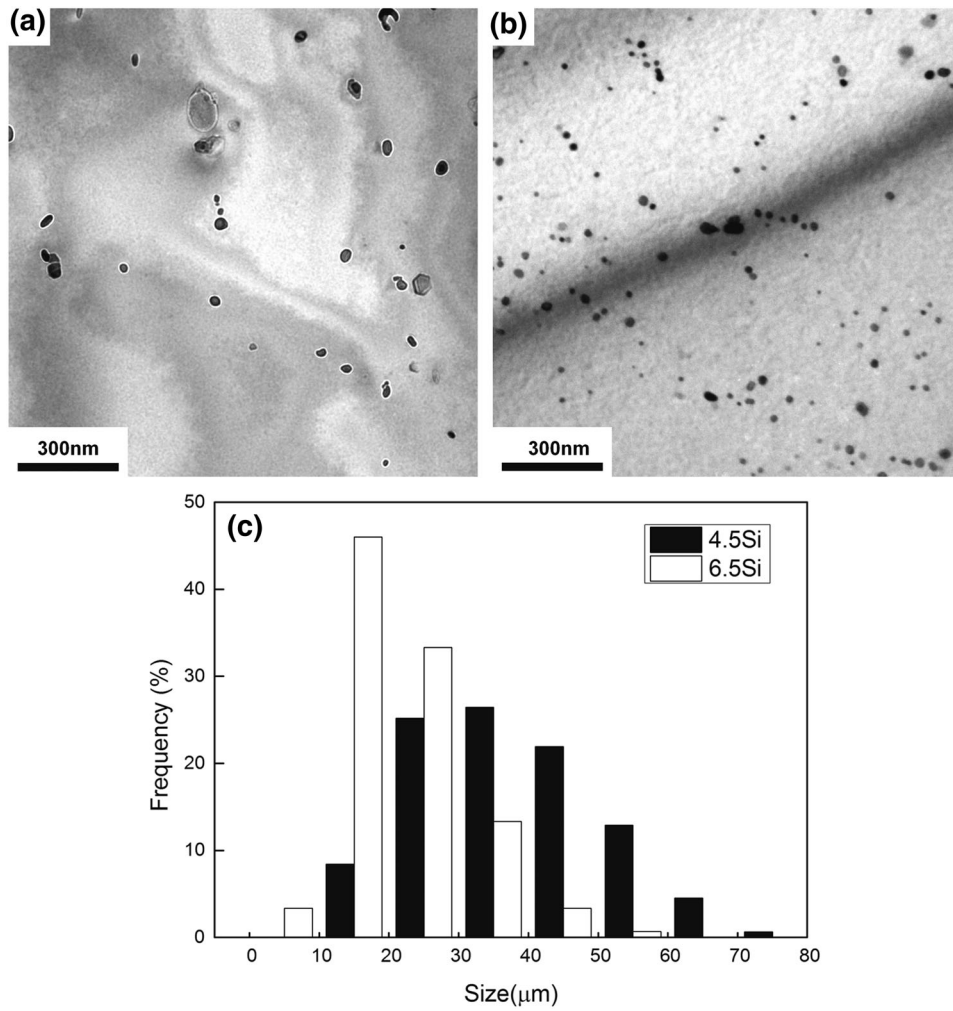


Fig. 7 Precipitates in primary annealed the 4.5Si steel **a**, the 6.5Si steel **b** and the particles size distribution **c**

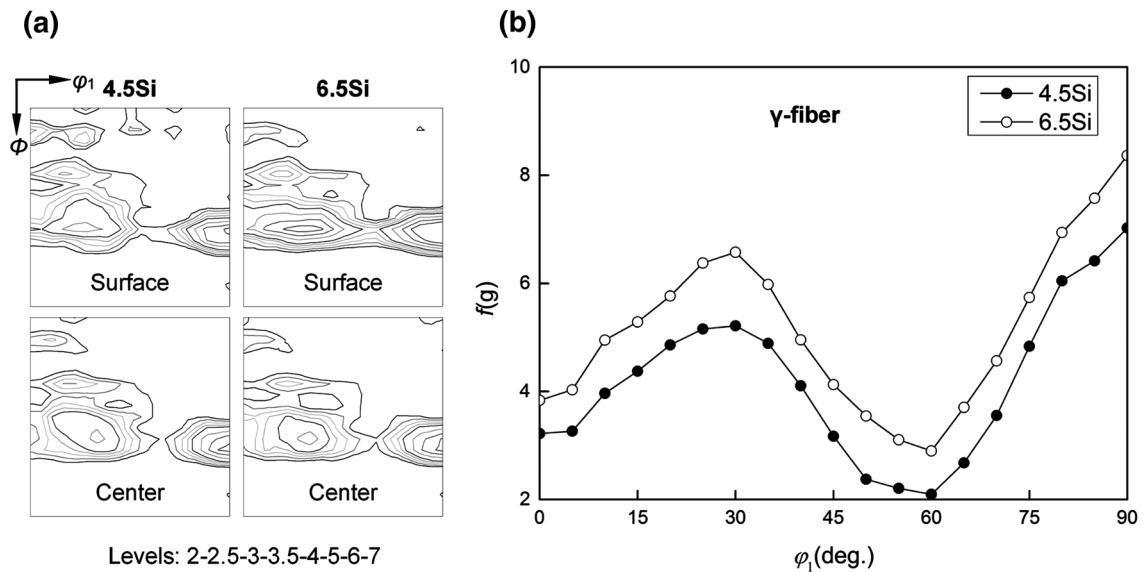


Fig. 8 Texture **a** and γ -fiber texture averaged over surface and center layer **b** of the 4.5Si and the 6.5Si steels after primary annealing

rolled sheet of the 6.5Si steel. It should be mentioned that three-stage rolling for the 4.5Si steel was adopted just for comparison. Indeed, the 4.5Si as-cast strip could be deformed at relatively low temperatures in the range of 100–300 °C.

Figure 3 illustrates the textures of final cold-rolled sheets. Similar textures containing α -fiber and γ -fiber were observed in both the 4.5Si and the 6.5Si steels. The peaks corresponded to $\{001\}\langle 110\rangle$, $\{112\}\langle 110\rangle$, and $\{111\}\langle 110\rangle$. In the 4.5Si steel, a pronounced texture gradient was exhibited through the thickness. Strong $\{001\}\langle 110\rangle$ and $\{112\}\langle 110\rangle$ textures were developed in the surface layer and decreased to moderate intensity in the center layer. Furthermore, strong rotated Goss orientation ($\{110\}\langle 110\rangle$) was observed in the surface layer and became weak in the center. Comparatively, the 6.5Si steel showed relatively homogeneous texture from the surface to the center. This texture distribution is beneficial for homogenization of the microstructure and the texture during the subsequent annealing process.

3.2 Primary Annealing

Figure 4 shows the microhardness evolution for the 4.5Si and the 6.5Si steels during primary annealing time from 5 to 100 s. It was clearly seen that for the 4.5Si steel, the primary recrystallization started at ~ 20 s and completed at ~ 40 s. For the 6.5Si steel, the primary recrystallization started at ~ 50 s and completed at ~ 70 s. It can be concluded that the 6.5Si steel had a recrystallization delay of ~ 30 s compared to the 4.5Si steel. It was interesting to note that when the annealing time was greater than 70 s, the microhardness of the 6.5Si specimen was increased. This is related to the reordered phenomena during

annealing [28]. Figure 5 shows the final microstructure of the 4.5Si and the 6.5Si steels after primary annealing (for 5 min). Both samples exhibited fully recrystallized equiaxed grains with an average grain size of ~ 14 and ~ 11 μm , respectively.

Surprisingly, the 6.5Si steel is expected to recrystallize faster than the 4.5Si steel because the presence of super dislocations in the 6.5Si steel retards dynamic recovery during warm deformation and restores higher energy in the final cold-rolled sheet. XRD studies were carried out to examine the store energy by using the method mentioned in Lee's work [29], and the result is presented in Fig. 6. The full width at half maximum (FWHM) of the 6.5Si specimen was broader than the 4.5Si specimens, confirming the higher store energy in the 6.5Si deformed samples. The peak of the 6.5Si specimens shifted to a higher angle due to the decrease in cell constant as a consequence of more substitution Si atoms in the 6.5Si steel. It can be concluded that stored energy plays a minor role in the determination of recrystallization rate, and other factors may be important.

Figure 7 shows typical TEM micrographs of the second-phase particles in the primary annealed sheets and their size distribution. These particles were mainly identified as compound of MnS, AlN, and NbN. Besides, few separated AlN and NbN precipitates were observed. In the 4.5Si steel, the size of the particles was in the range of 30–50 nm, and the average diameter was ~ 33 nm (Fig. 7a, c). In contrast, more particles were observed in the 6.5Si steel, and the size of the particles was in the range of 10–30 nm with an average diameter of ~ 22 nm (Fig. 7b, c). These second-phase particles play a key role in inhibiting normal grain growth during primary annealing and subsequent secondary annealing.

Considering the distinct distribution of the precipitates in the 4.5Si and the 6.5Si steels, the anomalous primary recrystallization rate can be elucidated. During primary annealing, recovery, which results in subgrains by annihilation and rearrangement of dislocations, usually occurs prior to the recrystallization process. These subgrains will coarsen and form recrystallized grains. In general, this process is delayed in the presence of second-phase particles because of the drag force. In the 6.5Si steel, more and finer dispersed second-phase particles introduce larger drag force to exert on the dislocations, suppressing recrystallization nuclei. On the other hand, after the recrystallization nuclei are formed, the second-phase particles will drag the grain boundaries for migration which is referred as Zener pinning effect [30]. This pinning effect is proportional to the volume fraction (f) and inversely proportional to the diameter (r) of second-phase particles. In comparison with the 4.5Si steel, the 6.5Si steel shows larger f and smaller r , meaning that larger pinning pressure is obtained, which

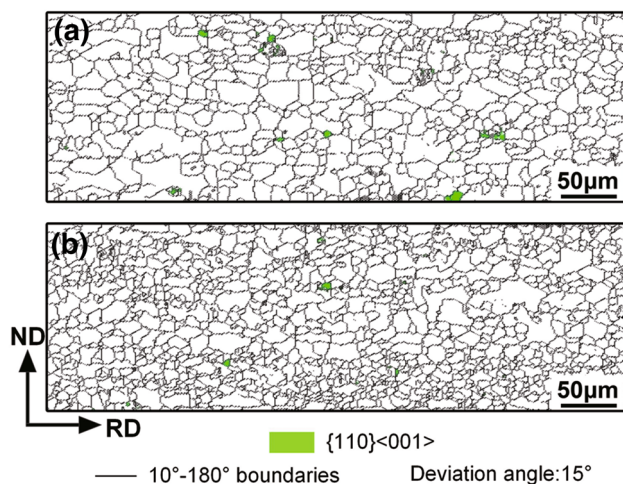


Fig. 9 Goss grains in the 4.5Si **a** and the 6.5Si **b** primary annealed sheets

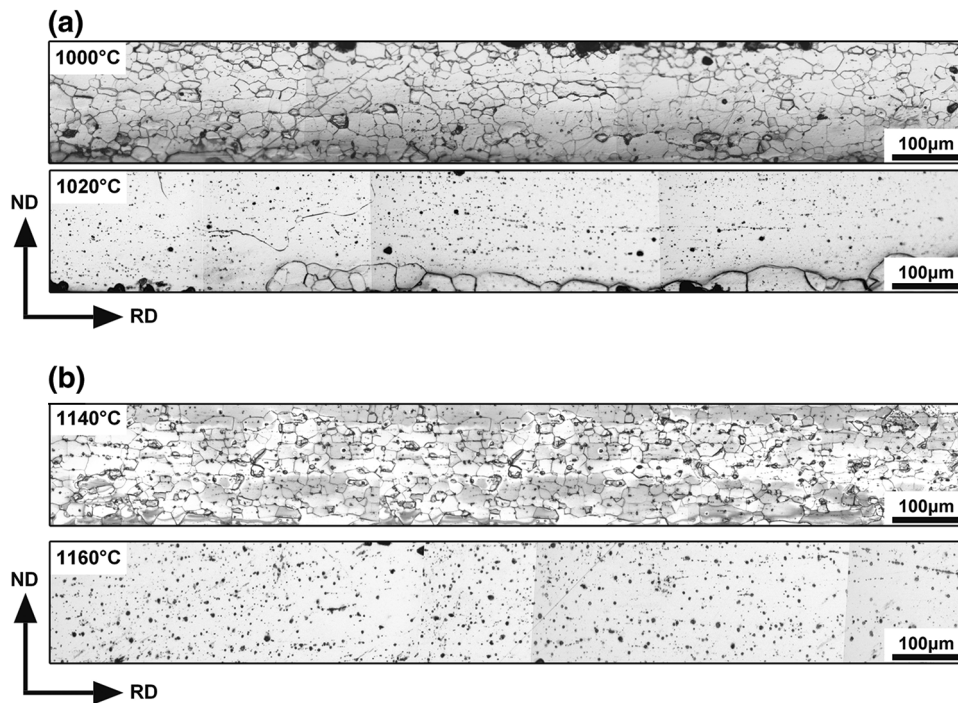


Fig. 10 Microstructures of samples for the 4.5Si **a** and the 6.5Si **b** steels

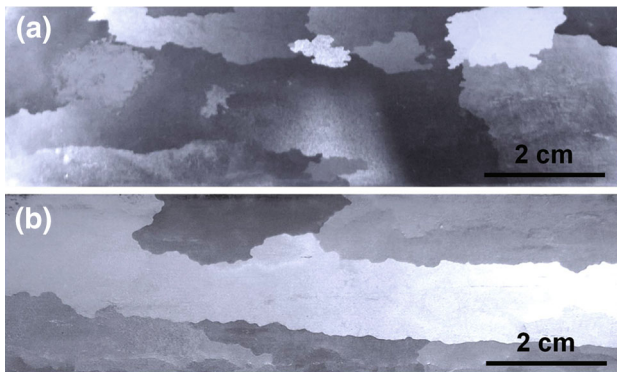


Fig. 11 Macrostructures of the 4.5Si **a** and the 6.5Si **b** steels after secondary recrystallization

reduces the recrystallization rate. In conclusion, more and finer second-phase particles in the 6.5Si steel decrease the recrystallization nucleation rate and nuclei coarsening rate, leading to ~ 30 -s delay in recrystallization.

Figure 8 shows the primary textures of both the 4.5Si and the 6.5Si steels. Strong γ -fiber with the maximum intensity at $\{111\}\langle 112\rangle$ was displayed in both steels, along with some weak scattering from $\{111\}\langle 112\rangle$ toward $\{554\}\langle 335\rangle$. Contrary to the results reported by Li *et al.* [19], weak λ -fiber texture was displayed, attributing to the random texture distribution in the as-cast strip and large rolling reduction before primary annealing in the present study. A comparison between the 4.5Si and the 6.5Si steels

clearly indicates that the latter has stronger $\{111\}\langle 112\rangle$ texture along the thickness, as shown in Fig. 8b. In general, $\{111\}\langle 112\rangle$ recrystallized grains are prone to form in the deform matrix and the grain boundaries, referred as “oriented nucleation” mechanism [31]. Gao *et al.* [32] demonstrated that the dominant $\{111\}\langle 110\rangle$ matrix prior to the annealing gave rise to the nucleation of $\{111\}\langle 112\rangle$ texture due to a special $30^\circ\langle 111\rangle$ orientation relationship. However, in the present study, the difference in the deformed $\{111\}\langle 110\rangle$ texture was much less significant (Fig. 3). Thus, it seems that the grain boundaries play a key role in defining texture. As shown in Fig. 1f, the 6.5Si cold-rolled sheet showed narrower pancake-shaped grain structure together with more grain boundaries. This means that more nucleation sites are available in the 6.5Si steel, leading to a strong $\{111\}\langle 112\rangle$ recrystallization texture.

Another pronounced characteristic of the present primary texture is the absence of Goss orientation, which is considered as the secondary nuclei during the subsequent secondary annealing. This distinct phenomenon can be explained in two aspects. First, non-hot rolling was adopted in the present work, reducing the original Goss orientation since Goss orientation strongly depends on shear deformation during hot rolling [33]. Second, the matrix for primary Goss nuclei during annealing was destroyed by relatively large rolling reduction. As is reported previously [34], a moderate rolling reduction (60–70%) prior to primary annealing is favorable for Goss nuclei during primary

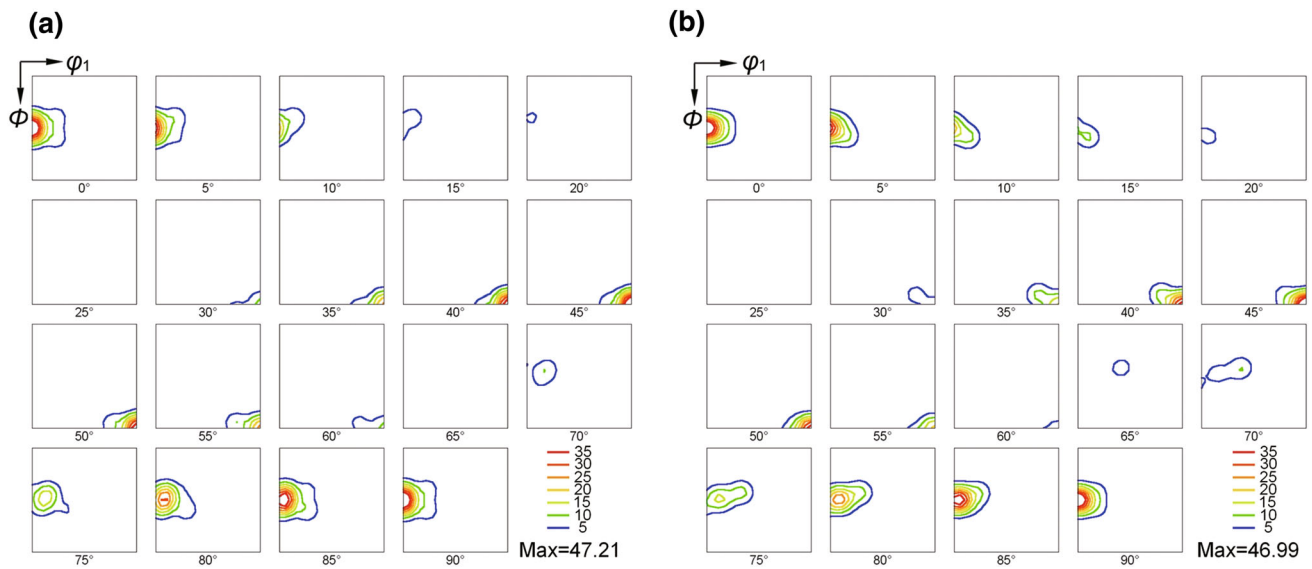


Fig. 12 Textures of secondary annealed sheets for the 4.5Si **a** and the 6.5Si **b** steels

Table 2 Magnetic properties of the high silicon steels

Material	Thickness (mm)	B_8 (T)	$P_{10/400}$ (W/kg)	$P_{10/1K}$ (W/kg)	Ref.
Grain-oriented 4.5% Si steel (strip cast)	0.20	1.75	10.21	42.37	This work
Grain-oriented 6.5% Si steel (strip cast)	0.20	1.76	8.659	32.24	This work
Non-grain-oriented 6.5% Si steel (CVD)	0.20	1.09	14.5	51.6	JNHF-Core [36]

annealing. However, a relatively large rolling reduction ($\sim 91\%$) was obtained in the present work, which further reduced the primary Goss orientation.

Because primary Goss grain was of importance during subsequent secondary annealing, EBSD studies were performed on the primary annealed sheets in order to confirm their presence. Figure 9 illustrates the typical EBSD maps, showing the distribution of Goss orientation in both the 4.5Si and the 6.5Si primary annealed sheets. The area fraction of Goss orientation in the 4.5Si steel was 0.8%, which was too small to be detected by macro-texture measurement. In contrast, fewer primary Goss orientation was shown in the 6.5Si steel, and the area fraction was about 0.1%.

3.3 Secondary Annealing

Figure 10 shows the cross-sectional microstructures of the extracted specimens. In the 4.5Si steel, the grains were equiaxed at 1000 °C and abnormally grown at 1020 °C, indicating the onset of secondary recrystallization occurred between 1000 and 1020 °C (Fig. 10a). In the case of the 6.5Si steel, the equiaxed grain structure was observed until 1140 °C and changed to abnormally grown grain structure at 1160 °C. This means that the secondary recrystallization occurs at the temperature higher than 1140 °C. The present

result was not difficult to understand when considering the second-phase particles in the primary annealed sheets. The 6.5Si steel indicated more and finer second-phase particles compared to the 4.5Si steel. Thus, a higher temperature and longer time were required for the onset of abnormal grain growth.

Figure 11 shows the final macrostructures of the 4.5Si and the 6.5Si steels after secondary recrystallization. The crystal orientation of these abnormal grown grains was identified as Goss orientation ($\{110\}\langle 001\rangle$) by EBSD, and indicated by the calculated constant- φ_2 ODF sections in Fig. 12. It was of interest to note that the 6.5Si steel had a larger grain size than the 4.5Si steel. On one hand, fewer Goss nuclei were shown in the primary annealed 6.5Si steel as indicated by EBSD results (Fig. 9). Thus, adequate abnormal grain grown for each Goss nuclei can be obtained before they contact the neighboring grains, which resulted in a larger final grain size. On the other hand, stronger $\{111\}\langle 112\rangle$ texture in the primary annealed 6.5Si steel enhanced the motion of Goss grain boundaries due to the special $35^\circ\langle 110\rangle$ orientation relationship between them [35], leading to a larger grain size in the 6.5Si steel after secondary recrystallization.

The presence of the desirable grain structure and texture in the 4.5Si and the 6.5Si final sheets indicated superior

magnetic properties, as shown in Table 2. The magnetic induction (B_8) approached 1.75 T and 1.76 T for the 4.5Si and the 6.5Si steels, which was much higher than the non-oriented 6.5% Si steel produced by CVD method [36]. The core losses in the 4.5Si steel at 400 Hz and 1000 Hz were higher than that of the 6.5Si steel and were obviously lower than that of the non-oriented 6.5 wt% Si steel. It can be concluded that the strip casting method is a viable way to produce grain-oriented high silicon steels.

4 Conclusions

- (1) After warm rolling at 700 °C, elongated grains together with massive shear bands were observed in the steel containing 6.5 wt% Si. In contrast, the shear bands were rarely observed in the 4.5 wt% Si steel.
- (2) During primary annealing, the onset of recrystallization in the steel containing 6.5 wt% Si occurred ~30 s later, and the final grain size was smaller than the 4.5 wt% Si steel. Moreover, fewer primary Goss grains were observed in the steel containing 6.5 wt% Si.
- (3) After secondary annealing, abnormal grain growth occurred in both the 4.5 wt% Si and the 6.5 wt% Si steels. Compared to the 4.5 wt% Si steel, abnormal grain growth in the 6.5 wt% Si steel occurred later, and the final grain size was significantly larger.
- (4) The magnetic induction B_8 for the 4.5 wt% Si and the 6.5 wt% Si steels was 1.75 T and 1.76 T, respectively. The core losses at 400 Hz and 1000 Hz by 1.0 T were lower than non-oriented 6.5 wt% Si steel produced by CVD method.

Acknowledgments The authors gratefully acknowledge the support from R. D. K. Misra, University of Texas at El Paso. This work was financially supported by the National Natural Science Foundation of China (Nos. 51174059, 51404155, and U1260204), the Fundamental Research Funds for the Central Universities (N130407003), the Program for New Century Excellent Talents in University (NCET-13-0111), and the Program for Liaoning Excellent Talents in University (LR2014007).

References

- [1] M.F. Littman, *J. Magn. Magn. Mater.* **26**, 1 (1982)

- [2] Z. Xia, Y. Kang, Q. Wang, *J. Magn. Magn. Mater.* **320**, 3229 (2008)
- [3] M.A. Cunha, G.W. Johnson, *J. Mater. Sci.* **25**, 2481 (1990)
- [4] C. Bolfarini, M.C.A. Silva, A.M. Jorge Jr, C.S. Kiminami, W.J. Botta, *J. Magn. Magn. Mater.* **320**, 653 (2008)
- [5] H. Honma, Y. Ushigami, Y. Suga, *J. Appl. Phys.* **70**, 6259 (1991)
- [6] K.I. Arai, K. Ishiyama, *J. Magn. Magn. Mater.* **133**, 233 (1994)
- [7] K.I. Arai, Y. Yamashiro, *J. Appl. Phys.* **64**, 5373 (1988)
- [8] U. Yoshiyuki, H. Hodaka, K. Shuji, S. Yozo, Japanese Patent 04,080,321 (1992)
- [9] S. Yozo, Japanese Patent 04,362,134 (1992)
- [10] N. Ujihiro, T. Makoto, I. Masayoshi, Japanese Patent 05,098,398 (1993)
- [11] T. Yasushi, O. Yoshihiko, Japanese Patent 2,003,064,420 (2003)
- [12] T. Minoru, H. Tatsuhiko, Japanese Patent 2,008,169,450 (2008)
- [13] H. Jung, J. Kim, *J. Magn. Magn. Mater.* **353**, 76 (2014)
- [14] H. Jung, M. Na, J.Y. Soh, S.B. Kim, J. Kim, *ISIJ Int.* **52**, 530 (2012)
- [15] J.Y. Park, K.H. Oh, H.Y. Ra, *Scr. Mater.* **40**, 881 (1999)
- [16] J.Y. Park, K.H. Oh, H.Y. Ra, *ISIJ Int.* **40**, 1210 (2000)
- [17] J.Y. Park, K.H. Oh, H.Y. Ra, *ISIJ Int.* **41**, 70 (2001)
- [18] H.-T. Liu, Z.-Y. Liu, Y.-Q. Qiu, Y. Sun, G.-D. Wang, *J. Mater. Process. Technol.* **212**, 1941 (2012)
- [19] H.Z. Li, H.T. Liu, Z.Y. Liu, H.H. Lu, H.Y. Song, G.D. Wang, *Mater. Charact.* **88**, 1 (2014)
- [20] Y.X. Zhang, Y.B. Xu, H.T. Liu, C.G. Li, G.M. Cao, Z.Y. Liu, G.D. Wang, *J. Magn. Magn. Mater.* **324**, 3328 (2012)
- [21] Y. Wang, Y.-B. Xu, Y.-X. Zhang, F. Fang, X. Lu, H.-T. Liu, G.-D. Wang, *J. Magn. Magn. Mater.* **379**, 161 (2015)
- [22] J. Ma, Y. Yang, W. Tong, *Acta Metall. Sin.* **43**, 879 (2007). (**in Chinese**)
- [23] H. Okamoto, *Phase Diagrams of Binary Iron Alloys* (ASM Intl, Almere, 1993)
- [24] F.J. Humphreys, M. Hatherly, *Recrystallization and Related Annealing Phenomena*, 2nd edn. (Elsevier, Oxford, 2004), p. 269
- [25] J. Ball, G. Gottstein, *Intermetallics* **1**, 171 (1993)
- [26] Y. Kaneno, A. Takahashi, T. Takasugi, *Mater. Sci. Eng. A* **431**, 328 (2006)
- [27] Y.D. Huang, L. Froyen, *Intermetallics* **10**, 473 (2002)
- [28] I. Baker, *Intermetallics* **8**, 1183 (2000)
- [29] S. Lee, B.C. De Cooman, *ISIJ Int.* **51**, 1545 (2011)
- [30] D. Raabe, in *Physical Metallurgy*, 5th edn., ed. by D.E.L. Hono (Elsevier, Oxford, 2014), p. 2291
- [31] J. Zhang, Y. Cao, G. Jiang, H. Di, *Acta Metall. Sin. (Engl. Lett.)* **27**, 395 (2014)
- [32] F. Gao, Z. Liu, H. Liu, G. Wang, *Acta Metall. Sin. (Engl. Lett.)* **24**, 343 (2011)
- [33] A. Böttcher, K. Lücke, *Acta Metall. Mater.* **41**, 2503 (1993)
- [34] M. Matsuo, *ISIJ Int.* **29**, 809 (1989)
- [35] H. Homma, B. Hutchinson, *Acta Mater.* **51**, 3795 (2003)
- [36] M. Namikawa, H. Ninomiya, T. Yamaji, *JFE Technol. Rep.* **6**, 12 (2005)